Jacob, *EMBO J.* **2**, 953 (1983); D. Jackson and P. Cook, *ibid.* **7**, 3667 (1988).
5. S. A. Berman, S. Bursztajn, B. Bowen, W. Gilbert, *Science* **247**, 212 (1990).
6. K. C. Carter *et al.*, *ibid.* **259**, 1330 (1993).
7. K. C. Carter, K. L. Taneja, J. B. Lawrence, *J. Cell Biol.* **115**, 1191 (1991).
8. D. L. Spector, W. H. Schrier, H. Busch, *Biol. Cell* **49**, 1 (1983); S. Fakan, G. Leser, T. E. Martin, *J. Cell Biol.* **98**, 358 (1984); N. Ringertz *et al.*, *J. Cell Sci. Suppl.* **4**, 11 (1986); J. D. Northway and E. M. Tan, *Clin. Immunol. Immunopathol.* **1**, 140 (1972).
9. X.-D. Fu and T. Maniatis, *Nature* **343**, 437 (1990).
10. J. Wang, L. Cao, Y. Wang, T. Pederson, *Proc. Natl. Acad. Sci. U.S.A.* **88**, 7391 (1991).
11. J. B. Lawrence, L. M. Marselle, K. S. Byron, J. L. Sullivan, R. H. Singer, *ibid.* **87**, 5420 (1990); A. Raap *et al.*, *Exp. Cell Res.* **197**, 319 (1991).
12. S. Huang and D. L. Spector, *Genes Dev.* **5**, 2228 (1991).
13. P. R. Dobner, A. S. Tischler, Y. C. Lee, S. R. Bloom, S. R. Donahue, *J. Biol. Chem.* **263**, 13983 (1988); E. Kislauskis, B. Bullock, S. McNeil, P. R. Dobner, *ibid.*, p. 4963; M. J. Alexander *et al.*, *Proc. Natl. Acad. Sci. U.S.A.* **86**, 5202 (1989).
14. J. E. Schwarzbauer, R. S. Patel, D. Fonda, R. O. Hynes, *EMBO J.* **6**, 2573 (1987); R. S. Patel, E. Odermatt, J. E. Schwarzbauer, R. O. Hynes, *ibid.*, p. 2565.
15. The methods used here extend a series of studies aimed at improving the preservation and detection of nuclear RNA and DNA in situ [J. B. Lawrence, C. A. Villnave, R. H. Singer, *Cell* **52**, 51 (1988); (*2, 3, 7, 20*)]. For studies on fibronectin RNA, cells were grown and analyzed as monolayers on glass cover slips. Before hybridization, cells were treated for 30 s with 0.5% Triton X-100 in cytoskeleton buffer [E. G. Fey, G. Krochmalinc, S. Penman, *J. Biol. Chem.* **102**, 1654 (1986)] at 4°C to permeabilize nuclei and were then fixed in 4% paraformaldehyde and 1× phosphate-buffered saline for 5 min at room temperature. Cells were stored in 70% ethanol at 4°C before hybridization. Rat PC-12 cells were induced to express neurotensin (*13*) by the addition of nerve growth factor (100 ng/ml), 1 μM Dexamethasone (Sigma), 1 μM forskolin (Sigma), and 10 mM LiCl. Because PC-12 cells have little cytoplasm and are nonadherent on glass, they did not require detergent treatment but were spun from suspension onto cover slips for 5 min at 500 rpm and fixed in 4% paraformaldehyde for 5 to 10 min. Hybridization with the fibronectin and neurotensin probes was performed essentially as described (*2, 20*) with the probe (5 μg/ml) in 50% formamide 2× saline sodium citrate (SSC) for 4 to 16 hours at 37°C. For simultaneous detection of fibronectin RNA and poly(A) RNA, the cDNA probe for fibronectin (pFH-1) was hybridized first and then the oligo(dT) [deoxy$(T)_{55}$; 0.5 μg/ml] was hybridized in 15% formamide and 2× SSC at 37°C for 2 to 3 hours. The monoclonal antibody to SC-35 was used at 37°C for 60 min and then detected with a rhodamine-conjugated donkey antibody to murine immunoglobulin (Jackson ImmunoResearch Labs). Several points support the conclusion that the methods specifically detect nuclear RNA. In the absence of denaturation before hybridization, double-stranded cellular DNA is unavailable for hybridization (*2, 20*). Consistent with this observation in the inducible system (neurotensin), the noninduced cells showed no nuclear signal, and in the fibronectin system, the nuclear RNA signals were removed by alkaline hydrolysis of RNA with NaOH. The larger RNA signals relative to single-copy gene signals and the coincidence in expression of nuclear and cytoplasmic RNA signals provide further evidence that we are detecting nuclear RNA.
16. We have investigated nuclear localization of several other RNAs, including six different viral and cellular precursor mRNAs in different cultured cell types, and have not found evidence for a specific orientation of the RNA tracks. In randomly rotated suspension cells, RNA foci artifactually appeared oriented in the *z* axis because of the limited *z* axis resolution of the confocal microscope. Separation of specific sequences along viral RNA tracks has also been observed (J. B. Lawrence and J. Bauman, unpublished data).
17. As has been documented in detail [J. B. Lawrence, R. H. Singer, J. A. McNeil, *Science* **249**, 928 (1990); B. Trask, D. Pinkel, G. van den Engh, *Genomics* **5**, 710 (1989)], the length of individual genes within interphase nuclei is generally below the resolution of the light microscope (0.1 to 0.2 μm). Even sequences separated by 70 kb (the full length of the fibronectin gene) are less than 0.2 μm apart in approximately 90% of nuclei and therefore appear as a single, small spot.
18. O. L. Miller, Jr., and B. R. Beatty, *Science* **164**, 955 (1969); Y. O. Osheim, O. L. Miller, A. L. Beyer, *Cell* **43**, 143 (1985).
19. J. R. Nevins, *Annu. Rev. Biochem.* **52**, 441 (1983); A. L. Beyer and Y. N. Osheim, *Semin. Cell Biol.* **2**, 131 (1991). There is evidence for and against the cotranscriptional splicing of precursor mRNAs. Beyer has shown that nascent transcripts in *Drosophila* are associated with spliceosomes, and in some cases, the spliceosome and nascent transcripts can be directly visualized by electron microscopy. In contrast, Nevins and others have shown that the unspliced transcripts in mammalian cells can be isolated in the poly(A) fraction, which indicates that splicing is posttranscriptional.
20. C. V. Johnson, J. A. McNeil, K. C. Carter, J. B. Lawrence, *Genet. Anal. Tech. Appl.* **8**, 75 (1991). The two-color filter was made by Chroma Technology, Brattleboro, VT; C. V. Johnson, R. Singer, J. R. Lawrence, *Methods Cell Biol.* **35**, 73 (1992).
21. D. C. Tkachuk *et al.*, *Science* **250**, 559 (1990).
22. Because of their abundant cytoplasm, fibroblasts and myoblasts were extracted with Triton X-100, a treatment that may preferentially release excised intron sequences from the nucleus (*23*). The presence of fibronectin mRNA in the fibroblast perinuclear cytoplasm made it difficult to evaluate whether there was a low concentration of exons throughout the nucleoplasm. The PC-12 cells were easier to evaluate because they have little cytoplasm and did not need to be detergent-extracted.
23. S. Zeitlin, A. Parent, S. Silverstein, A. Efstratiadis, *Mol. Cell. Biol.* **7**, 111 (1987); C. Coleclough and D. Wood, *ibid.* **4**, 2017 (1984).
24. The nuclear volume occupied by all of the poly(A) domains in a given nucleus is estimated to be 5% (*6*), whereas the specific RNA accumulations occupy no more than 1%. Hence, the frequency with which fibronectin RNA would spatially associate with these domains by random chance is small. The specificity of association is further demonstrated by previous experiments showing that nontranscribed centromeric sequences are not associated with poly(A) domains (*7*).
25. Because poly(A) RNA is detected with a small (55 bp) oligonucleotide end-labeled with only a few biotin molecules and the fibronectin RNA is detected by much larger (1 to 6 kb) probes labeled throughout by nick-translation, the amount of fluorescence generated per molecule with the poly(A) probe is much less (at least an order of magnitude) than that generated with the fibronectin mRNA probe. Nevertheless, rough measurements of the relative intensity and size of individual poly(A) RNA domains indicate that the domains contain substantially more fluorescent signal (and hence many more RNA molecules) than individual RNA foci or tracks do. This consideration, along with the observation that fibronectin RNA tracks only partially overlap the transcript domains, supports the conclusion that each transcript domain is likely to be the transcription and processing site of several RNAs.
26. J. R. Coleman and J. B. Lawrence, unpublished data; Y. Xing and J. B. Lawrence, unpublished data. Several but not all active sequences studied are associated with domains.
27. We thank R. Hynes, J. Schwarzbauer, D. Shapiro, and P. Norton for providing SX19-3 and C1A1, BBG-5′BR, pFH-1, and G1-4.9 clones, respectively; T. Maniatis for supplying antibody to SC-35; C. Beaudry for help with manuscript preparation; C. Dunshee for excellent and patient assistance in photographic processing; and J. McNeil for expertise in computer imaging. Supported by Research Career Development Award grant from NIH National Center for Human Genome Research (J.B.L.), by NIH grant RO1 HG00251 (J.B.L.), and by NIH grant RO1 HL33307 (P.R.D.).

14 July 1992; accepted 22 December 1992

A Three-Dimensional View of Precursor Messenger RNA Metabolism Within the Mammalian Nucleus

Kenneth C. Carter, Douglas Bowman, Walter Carrington, Kevin Fogarty, John A. McNeil, Fredric S. Fay, Jeanne Bentley Lawrence*

A quantitative three-dimensional analysis of nuclear components involved in precursor messenger RNA metabolism was performed with a combination of fluorescence hybridization, immunofluorescence, and digital imaging microscopy. Polyadenylate [poly(A)] RNA-rich transcript domains were discrete, internal nuclear regions that formed a ventrally positioned horizontal array in monolayer cells. A dimmer, sometimes strand-like, poly(A) RNA signal was dispersed throughout the nucleoplasm. Spliceosome assembly factor SC-35 localized within the center of individual domains. These data support a nuclear model in which there is a specific topological arrangement of noncontiguous centers involved in precursor messenger RNA metabolism, from which RNA transport toward the nuclear envelope radiates.

Nuclei of higher eukaryotic cells must transcribe, process, and selectively transport several major classes of RNA including mRNA, ribosomal RNA (rRNA), tRNA, and small nuclear RNA. The transcription and processing of rRNA are confined to the nucleolus (*1*), but the subnuclear location of metabolism for other RNA classes including precursor mRNA (pre-mRNA) remains unresolved (*2–10*). Recent evidence

has emerged for subnuclear regions that contain large amounts of different classes of RNAs and specific proteins involved in RNA metabolism (6–15). By fluorescence in situ hybridization (10), we showed previously that nuclear poly(A) RNA, which represents approximately 90% of all pre-mRNA (16), has a clustered nuclear distribution that coincides with the distribution of small nuclear ribonucleoproteins (snRNPs) of the pre-mRNA splicing class (9); these snRNPs have long been known to exhibit a "speckled" distribution pattern (6, 7). Both transcription and splicing of an individual RNA are associated with these poly(A) RNA-rich regions (17); this result raises the possibility that these regions contain clusters of active genes (9, 17, 18).

As shown for immunofluorescence of nuclear pores (Fig. 1), digital images from a standard wide-field microscope, when combined with an image restoration algorithm that removes out-of-focus light, allow for a highly accurate estimate of the molecular distribution of fluorescent samples and give the maximum spatial resolution obtainable by light microscopy (19). Here, we use this approach to study the three-dimensional (3-D) nuclear topography of pre-mRNA metabolism primarily in human diploid fibroblasts (HDFs) by specific detection of pre-mRNA, snRNPs, the non-snRNP splicing factor SC-35, nuclear pores, and total DNA (20).

Three-dimensional analysis of poly(A) RNA distribution in HDFs showed regions of intense signal that had considerable substructure, along with regions of much dimmer signal dispersed throughout the nucleoplasm, excluding nucleoli (Fig. 2, A and B). There were both quantitative and qualitative differences between these two populations of poly(A) RNA. The concentration of poly(A) RNA within the regions of intense signal was a minimum of tenfold and often several thousandfold higher than in the area encircling the region; thus, a flood-fill operation was used to define individual transcript domains (Fig. 2, E and F; these discrete domains were generally not connected by the dimmer dispersed signal). There were 20 to 40 such domains per nucleus, ranging in diameter from ~0.5 to 3 μm (areas of intense signal that were <0.5 μm in diameter were not designated as transcript domains). The splicing factor SC-35, shown to be highly concentrated in these regions (13), was even more discretely localized than poly(A) RNA and did not produce a dimmer signal dispersed throughout the nucleoplasm (Fig. 2, C, D, and G). However, some cells had tiny punctate SC-35 signals in addition to the larger domains.

The distributions described above for poly(A) RNA and SC-35 were not unique to HDFs. Analyses of two different HDF strains (HDF and Detroit 551), HeLa cells, rat myoblast line L6 (all grown as monolayer cultures), and the lymphoma cell line Namalwa (grown in suspension) with probes for poly(A) RNA, snRNPs, or SC-35 indicated that the discrete nature of these domains is a feature of many cell types. However, the pattern varied somewhat depending on the cell type and metabolic state of the cells. For example, the SC-35 distribution in HeLa cells was comprised primarily of noncontiguous larger domains and often included smaller punctate signals (Fig. 2, H and I). Our results agree with previously reported two-dimensional images showing "speckles" of snRNPs (6, 7) that also contain SC-35 (13, 21) but do not agree with previous 3-D analyses and the interpretation of this pattern as a "nucleoplasmic reticulum" that is contiguous from the nucleolus to the nuclear envelope (21, 22). This discrepancy is not a result of differences in fixation methods (Fig. 2, H and I) but may be related to the enhanced quantitative capabilities and resolving power of the methods used here (23). The presence of a reticulum could suggest that RNA metabolism does not occur around discrete centers but instead occurs at any point along one continuous path involved in transport. In contrast, the independence of the domains we observed (which do not contact the nuclear envelope) suggests that there are centralized regions of RNA metabolism from which transport to the nuclear envelope radiates.

Analyses of the 3-D topography of transcript domains in HDFs showed that they were internally localized. In >95% of cells analyzed, they were aligned in a planar, horizontal array in the lower (ventral) por-

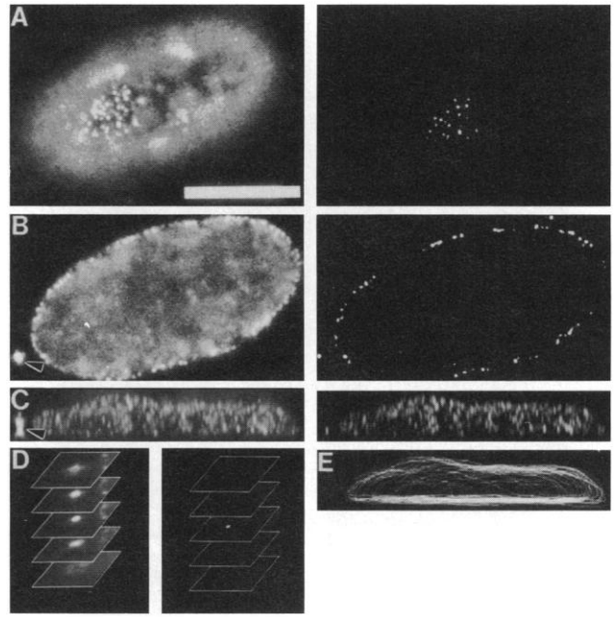

Fig. 1. Image restoration and analyses of 3-D images of nuclear pores. HDFs grown on cover slips were fixed in paraformaldehyde, and nuclear pores were visualized with a fluorochrome-conjugated antibody to the pore complex (31). A series of digitized images was taken of a cell (*z* axis spacing = 0.2 μm), and an image restoration (deconvolution) algorithm was then used to estimate the true distribution of the fluorescence in each plane (19, 20). This procedure permits visualization of the entire data set in three dimensions with out-of-focus light minimized and quantitative analysis of the fluorescence distribution. In (A) to (D), the original unprocessed image is on the left and the restored image is on the right (arrowhead denotes one of the fluorescent beads added to samples as alignment markers; bar = 10 μm). (**A** and **B**) Nuclear pore distribution in two focal planes before and after image restoration. (**C**) The entire 3-D data set showing the distribution of nuclear pores in a single cell before and after image restoration. The cell is shown from the side. The blurring of the image is largely but not fully reversed by the image restoration algorithm. For the 0.2-μm bead in this image, the full width at half maximum intensity after image restoration was approximately 0.60 μm in the *z* axis and 0.25 μm in the *x-y* axis [this is better resolution in all directions than can be obtained with a confocal microscope under optimal conditions (32)]. Both the bead and the nuclear pores look stretched in the *z* axis, which reflects a lower resolution of the restored images in the *z* axis than in the *x* and *y* axes. The algorithm is capable of restoring the image of a fluorescent bead of defined size even more precisely; however, we generally chose a higher smoothness setting (α) to avoid introducing grainy noise that occurs when restoring the finest details of the faintest portions of the images. (**D**) Higher magnification view of the light distribution created by the bead in (B) and (C) in five focal planes 0.6 μm apart. Note the faithful restoration of the spherical central image plane of the bead. (**E**) Contour lines representing the nuclear border; the drawing of these lines was guided by restored computationally defined centers of fluorescence intensity for nuclear pores.

K. C. Carter, J. A. McNeil, J. B. Lawrence, Department of Cell Biology, University of Massachusetts Medical Center, 55 Lake Avenue North, Worcester, MA 01655. D. Bowman, W. Carrington, K. Fogarty, F. S. Fay, The Biomedical Imaging Group and the Department of Physiology, University of Massachusetts Medical Center, Worcester, MA 01655.

*To whom correspondence should be addressed.

tion of the nucleus, just below the midline (Fig. 3) (*24*). In many cells, transcript domains surrounded nucleoli and in some but not all cases appeared to contact the nucleolar surface. This internally positioned horizontal array was seen in three separate cell lines grown as monolayer cultures. Although there were slight variations in their vertical position, individual transcript domains were never stacked on top of each other.

The location of sequential steps in pre-mRNA metabolism was further investigated by an examination of the relative distributions of poly(A) RNA, SC-35, snRNPs, and DNA. Transcript domains, as defined by poly(A) RNA distribution, consistently showed intense labeling with antibodies to

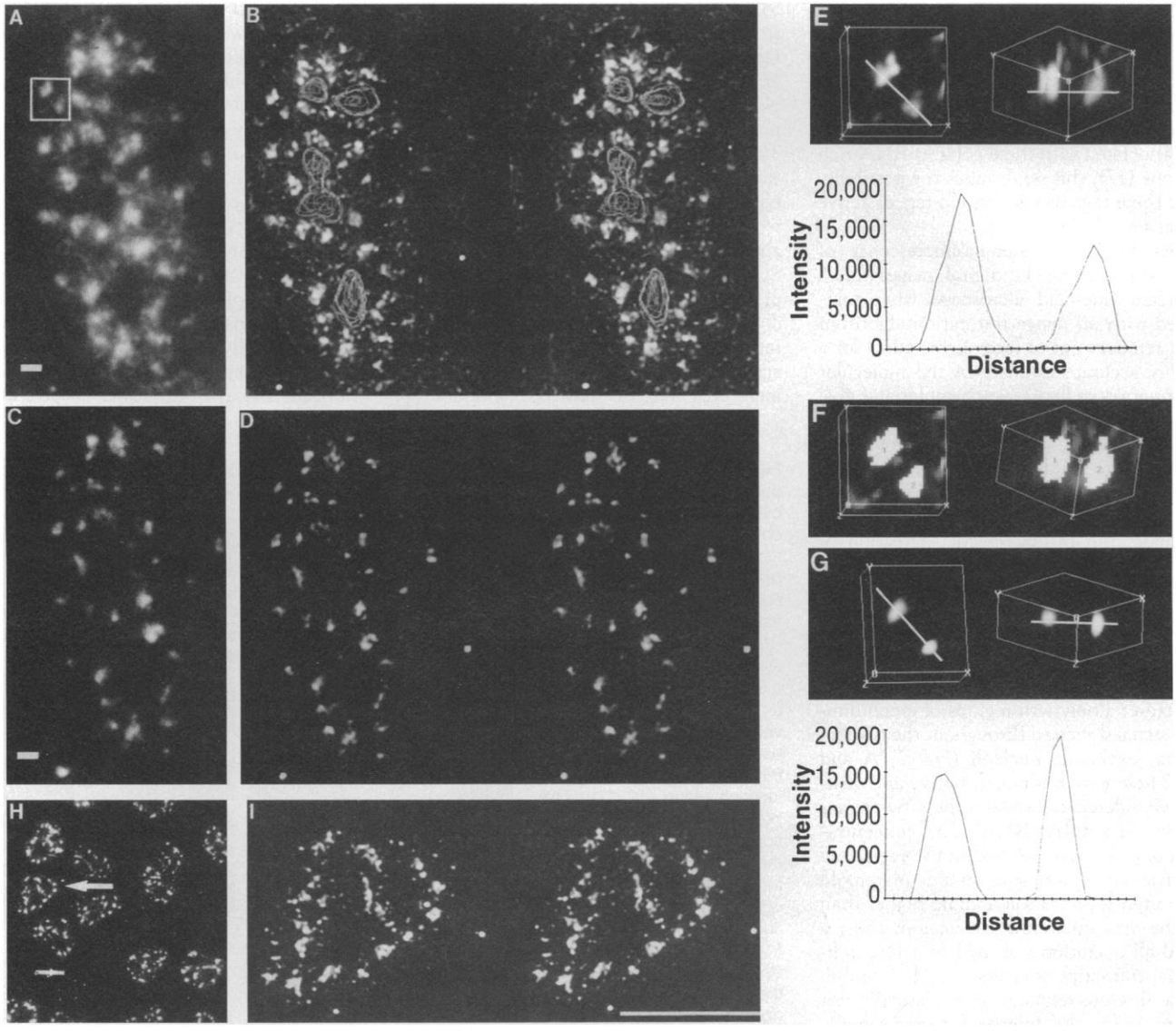

Fig. 2. Three-dimensional distribution of poly(A) RNA and SC-35. Poly(A) RNA and SC-35 were visualized simultaneously by fluorescence in situ hybridization and immunofluorescence (*31*), and data sets were acquired and restored as described in Fig. 1. Control experiments (*9, 31*) indicated that the nonuniform distribution of the poly(A) signal reflects the in vivo localization of this RNA and is not an artifact of fixation conditions, probe penetrability, or other experimental variables. The images shown are representative of the highly clustered pattern consistently seen in the majority of cells grown under normal conditions. (**A**) Poly(A) RNA in an HDF nucleus for a single-plane image from an unrestored data set (bar = 1 μm). Boxed area is shown in (E). (**B**) Restored stereopair image of entire data set for the cell in (A). The approximate positions of nucleoli are shown by contour lines. (**C**) SC-35 in the same cell as in (A) for a single-plane image from an unrestored data set (bar = 1 μm). (**D**) Restored stereopair image of entire data set from (C). (**E**) Quantitation of poly(A) RNA signal intensity in the restored image data set along a single (white) line from the area outlined by the box in (A). The boxed area is shown from two angles, and the postrestoration values at each voxel along the white line are indicated in the graph below. At the edge of each region of intense signal, the fluorescence intensity drops a minimum of one and usually two to three orders of magnitude throughout the area that encircles the domain. (**F**) On the basis of the quantitative drop at the edge of the concentrated regions of fluorescence, a threshold was set approximately one order of magnitude below the intensity within the region. A seed voxel was then selected from which a 3-D flood-fill operation expands the seed to include all voxels whose intensities are greater than the threshold (white area). Even when the threshold was set at or near 0 so that all trace signal leading from a domain was included, only rarely did the low-intensity signal extend from one domain to another. (**G**) Quantitation of SC-35 along a line in the same area as in (E). (**H**) Low-magnification view of unrestored SC-35 immunofluorescence in HeLa cells [fixed as in (*21*); bar = 10 μm]. (**I**) Image-restored data set of SC-35 distribution in a HeLa cell denoted by arrow in (H) shown as stereopair image (bar = 10 μm).

either SC-35 or snRNP antigens, as would be expected from the previously reported colocalization of poly(A) RNA and snRNPs (9) and of snRNPs and SC-35 (13). In our experiments, essentially all the domains that stained for SC-35 were also enriched in poly(A) RNA, the substrate for splicing (Fig. 4A). Because SC-35 is important for spliceosome assembly (11), its consistent colocalization with poly(A) RNA makes it unlikely that independent centers exist exclusively for the assembly or storage of spliceosomes and supports a view in which spliceosome assembly and splicing occur very close to one another. This is further supported by the finding that sites of active splicing are associated with transcript domains (17).

The transcript domains themselves appear to have a substructure in that SC-35 localized primarily to the central portion of each domain, forming a dense globular central core (Fig. 4, A and C). In contrast, snRNPs [detected with the antibody Y12, which immunoprecipitates the major snRNPs involved in pre-mRNA splicing plus several minor snRNPs of unknown function (25)] were localized throughout the transcript domains (Fig. 4D). The high concentration of both poly(A) RNA and snRNPs throughout the central region where SC-35 is highly concentrated (Fig. 4, A, C, and D) suggests that although spliceosome assembly may initiate or occur exclusively in the central core, RNA processing may also occur throughout the domain as well as adjacent to it. Foci of primary transcripts from some genes localize to the periphery of transcript domains (17), whereas the transcript foci of other genes occur directly within the central core (26).

Previous studies had indicated that regions rich in poly(A) RNA and splicing components lie within somewhat defined areas low in and possibly devoid of chromatin (9, 22). After image restoration, there was a substantial amount of DNA signal within transcript domains, comparable to the amount seen in nucleoli, which contain the decondensed and highly transcribed rRNA genes (Fig. 4B). Hence, there may be similarly decondensed DNA within transcript domains that may or may not be transcriptionally active. The discrete border of high-density chromatin that surrounds transcript domains often did not precisely correspond to the boundary of the poly(A) signal, leaving a gap that contained small amounts of DNA and no de-

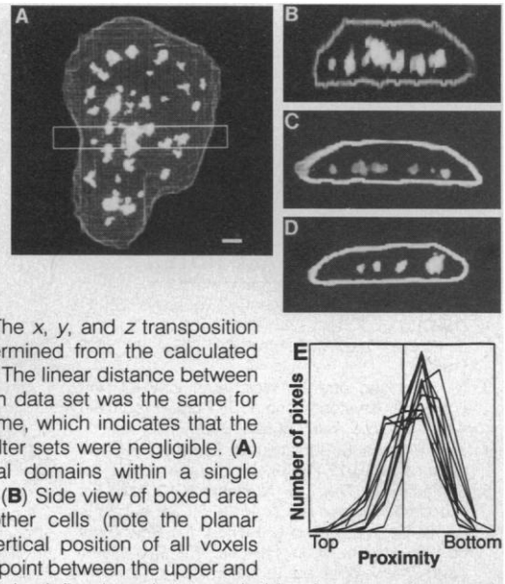

Fig. 3. Three-dimensional topography of transcript domains within individual HDF nuclei and their relation to the nuclear envelope. We obtained pairs of 3-D data sets by visualizing poly(A) RNA with Texas red and nuclear pores with fluorescein. After image restoration, the borders of individual transcript domains and the nuclear envelope were defined as described in Figs. 1 and 2. We then aligned data sets (with an accuracy of ±0.035 μm) in the *x*, *y*, and *z* axes by using beads visibly positioned near each cell through both Texas red or fluorescein filter sets. The *x*, *y*, and *z* transposition required to align the data sets was determined from the calculated centroids for these beads after restoration. The linear distance between the centroids of separate beads in a given data set was the same for Texas red and fluorescein >98% of the time, which indicates that the differences in magnification between the filter sets were negligible. (**A**) Position of nuclear border and individual domains within a single fibroblast nucleus (top view; bar = 1 μm). (**B**) Side view of boxed area in (A). (**C** and **D**) Side views for two other cells (note the planar distribution of transcript domains). (**E**) Vertical position of all voxels within transcript domains relative to the midpoint between the upper and lower nuclear envelope. The lower border is defined as the ventral side closest to the growth substrate. Data are from a total of 12 cells studied in three experiments. Similar results were obtained with antibodies to snRNPs or SC-35. On average, 81% of the transcript domain volume fell below the midline of the nucleus. Quantitative analyses indicated that the point on each domain closest to the border was 0.84 ± 0.34 μm. Collectively, transcript domains occupied <5% of the total nuclear volume.

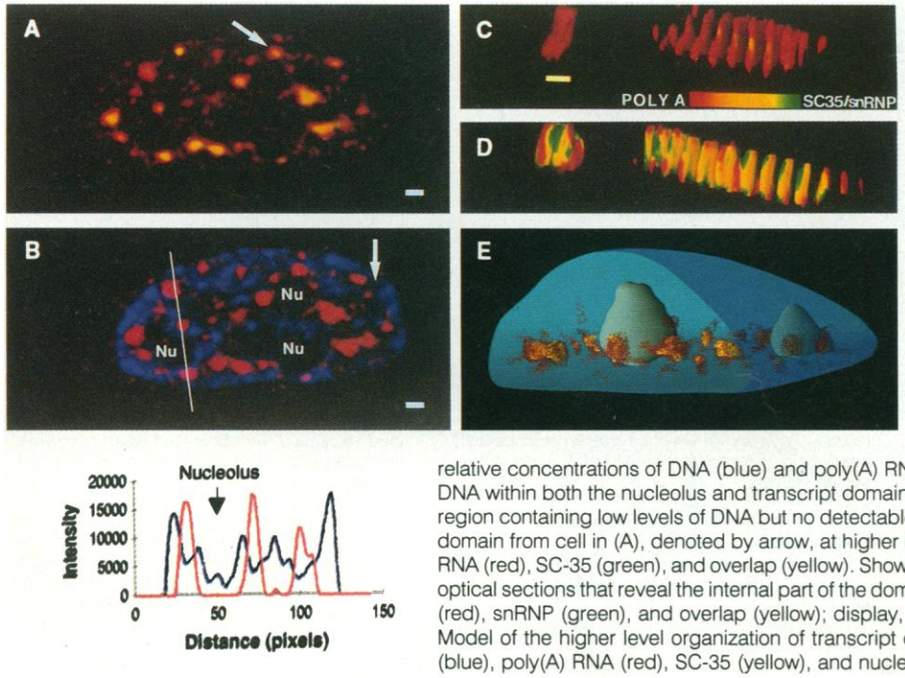

Fig. 4. Distribution of poly(A) RNA relative to SC-35, snRNP antigens, and DNA. (**A**) A 1-μm-wide *z* plane from the middle of an image-restored HDF nucleus showing poly(A) RNA (red) and splicing factor SC-35 (green). Substantial overlap is shown as yellow (alignment was performed as described in Fig. 3). Note that concentrations of SC-35 generally localized completely within transcript domains (bar = 1 μm). (**B**) A 1-μm-wide *z* plane from the middle of an image-restored nucleus showing poly(A) RNA (red), total DNA stained with 4,6-diamino-2-phenylindole (DAPI) (blue), and substantial overlap (pink) (Nu, nucleolus). Poly(A) RNA occupies much, but not all, of the nonnuclear areas with low levels of chromatin. Because of the large range of DAPI intensities, it is impossible to depict accurately both the very high and very low intensity areas in one photograph. The graph below (B) shows the relative concentrations of DNA (blue) and poly(A) RNA (red) along the white line in (B). Note that there is DNA within both the nucleolus and transcript domains along this line. [Arrow in (B) denotes a nonnuclear region containing low levels of DNA but no detectable poly(A) RNA; bar = 1 μm.] (**C**) Individual transcript domain from cell in (A), denoted by arrow, at higher magnification and from a side view, showing poly(A) RNA (red), SC-35 (green), and overlap (yellow). Shown are the intact domain (left; bar = 1 μm) and 0.2-μm optical sections that reveal the internal part of the domain (right). (**D**) A single domain showing poly(A) RNA (red), snRNP (green), and overlap (yellow); display, scaling, and coloration are as indicated for (C). (**E**) Model of the higher level organization of transcript domains within the nucleus. Overall nuclear volume (blue), poly(A) RNA (red), SC-35 (yellow), and nucleoli (gray) are shown.

tectable RNA (Fig. 4B). There were also other nonnucleolar regions that had small amounts of DNA but no detectable poly(A) RNA. These results support the hypothesis that transcript domains are structurally independent regions and not simply areas where RNA and splicing components are passively squeezed in between chromatin.

Because the RNAs produced within transcript domains must ultimately exit the nucleus, we investigated the position of the domains relative to the nuclear envelope. Our 3-D analyses revealed that the majority of domains were restricted to the interior portion of the nucleus (Fig. 3), with the closest point on individual domains averaging 0.8 μm from the nuclear border. Over 98% of the total domain volume was ≥1.5 μm away from the border. Thus, except for one domain in every two or three cells, transcript domains did not contact the nuclear border. Therefore, it seems unlikely that the pore complexes or laminae, which extend no more than 0.1 μm into the nuclear interior (*27*), interact directly with these domains.

How then do mature mRNAs reach nuclear pores? In restored images, the dimmer poly(A) RNA dispersed throughout the nucleoplasm often appeared strand-like (Fig. 2B). Although these strands frequently emanated from transcript domains and occasionally connected a domain with the nuclear border (Fig. 4, A and B), they were most often found as separate entities. In some cases, these strands coincided with sites of low DNA concentration. The relation between these minor strands of poly(A) RNA and tracks of single RNA species (*10, 17, 28*) remains to be determined. Because poly(A) RNA generally did not accumulate near the nuclear envelope, it seems unlikely that all mature messages in transit were visualized in these experiments. Transport to and through the nuclear pore does not appear to be rate-limiting.

Collectively, our results show discrete domains that are clearly implicated as centers of metabolic activity associated with RNA polymerase II transcripts. The finding of an internal core of SC-35, a protein essential for spliceosome assembly, suggests that individual transcript domains may have functional radial symmetry. Xing *et al.* (*17*) provide direct evidence that transcript domains are near or overlapping sites of both splicing and transcription by showing that tracks of individual RNA species overlap the position of the gene, are associated with individual domains, and are the site of intron removal. Our results indicate that spliceosome assembly may occur more centrally within each domain, whereas transcription and splicing could occur within the domain or at its periphery. Our data and those of Xing *et al.* (*17*) address the long-standing question of whether active chromatin is preferentially localized near the nuclear periphery to facilitate RNA transport (*2–5*) and support a model in which mRNA metabolism occurs more internally (Fig. 4E). The highly organized view of nuclear structure seen here is consistent with evidence indicating that RNA metabolism occurs in association with the nuclear matrix (*28, 29*). However, it is unclear how our results relate to electron microscopy studies of various nuclear structures (*30*) and how transcript domains correlate to large splicing factor–rich granules seen in amphibian oocytes (*14*). Finally, it will be of interest to learn how the overall organization of mRNA metabolism changes with, and may contribute to, the cell type–specific morphology and metabolic state of the cell.

REFERENCES AND NOTES

1. U. Sheer and R. Benavente, *BioEssays* **12**, 14 (1990).
2. G. Blobel, *Proc. Natl. Acad. Sci. U.S.A.* **82**, 8527 (1985).
3. N. Hutchison and H. Weintraub, *Cell* **43**, 471 (1985); A. Krystosek and T. T. Puck, *Proc. Natl. Acad. Sci. U.S.A.* **87**, 6560 (1990).
4. S. A. Berman, S. Bursztajn, B. Bowen, W. Gilbert, *Science* **247**, 212 (1990).
5. S. Fakan, in *The Cell Nucleus*, H. Busch, Ed. (Academic Press, New York, 1978), vol. V, part B, pp. 3–49; _____ and E. Puvion, *Int. Rev. Cytol.* **65**, 255 (1980); M. D. Fawcett, *The Cell* (Saunders, Philadelphia, ed. 2, 1981).
6. J. D. Northway and E. M. Tan, *Clin. Immunol. Immunopathol.* **1**, 140 (1972); D. L. Spector, W. H. Schrier, H. Busch, *Biol. Cell* **49**, 1 (1983); U. Nyman *et al.*, *J. Cell Biol.* **102**, 137 (1986); D. J. Elliot *et al.*, *EMBO J.* **11**, 3731 (1992).
7. S. Fakan, G. Leser, T. E. Martin, *J. Cell Biol.* **98**, 358 (1984).
8. J. Wang, L.-G. Cao, Y.-L. Wang, T. Pederson, *Proc. Natl. Acad. Sci. U.S.A.* **88**, 7391 (1991).
9. K. C. Carter, K. L. Taneja, J. B. Lawrence, *J. Cell Biol.* **115**, 1191 (1991).
10. J. B. Lawrence, C. A. Villnave, R. H. Singer, *Cell* **52**, 51 (1988); J. B. Lawrence, R. H. Singer, L. M. Marselle, *ibid.* **57**, 493 (1989).
11. S. Huang and D. L. Spector, *Proc. Natl. Acad. Sci. U.S.A.* **89**, 305 (1992).
12. M. Carmo-Fonseca *et al.*, *J. Cell Biol.* **117**, 1 (1992).
13. X.-D. Fu and T. Maniatis, *Nature* **343**, 437 (1990).
14. J. G. Gall and H. G. Callan, *Proc. Natl. Acad. Sci. U.S.A.* **86**, 6635 (1989); J. G. Gall, *Science* **252**, 1499 (1991).
15. Small nuclear RNAs of the pre-mRNA splicing class are highly concentrated within one to four small nuclear foci [M. Carmo-Fonseca *et al.*, *EMBO J.* **10**, 195 (1991); *ibid.*, p. 1863] called coiled bodies [I. Raska *et al.*, *Exp. Cell Res.* **195**, 27 (1991); D. S. Spector *et al.*, *Mol. Biol. Cell* **3**, 555 (1992); (*12*)] and within transcript domains–snRNP clusters (*11, 12*). Coiled bodies, whose function is unknown, might have an important function in pre-mRNA metabolism but do not contain large amounts of SC-35 (*11, 12*) or poly(A) RNA (K. C. Carter, C. V. Johnson, J. B. Lawrence, in preparation) and may not be major sites of splicing.
16. L. Puckett and J. E. Darnell, *J. Cell. Physiol.* **90**, 521 (1976); J. R. Nevins, *Annu. Rev. Biochem.* **52**, 441 (1983).
17. Y. Xing, C. V. Johnson, P. R. Dobner, J. B. Lawrence, *Science* **259**, 1326 (1993).
18. Several lines of evidence indicate a close spatial and temporal linkage between pre-mRNA transcription and processing [A. L. Beyer *et al.*, *Cell* **26**, 155 (1981); S. T. Smale and R. Tjian, *Mol. Cell. Biol.* **5**, 352 (1985); S. Fakan, G. Leser, T. E. Martin, *J. Cell Biol.* **103**, 1153 (1986)]. See also A. L. Beyer and Y. N. Osheim, *Semin. Cell Biol.* **2**, 131 (1991).
19. W. A. Carrington, *SPIE Proc.* **1205**, 72 (1990); W. A. Carrington *et al.*, in *Noninvasive Techniques in Cell Biology*, J. K. Foskett and S. Grinstein, Eds. (Wiley-Liss, New York, 1990), pp. 53–72.
20. Optical sections were obtained with a standard Zeiss microscope equipped with epifluorescence filters. Images were recorded with a cooled charge-coupled device (CCD) camera (Photometrics Inc.) with a pixel diameter of 20 μm and a dynamic range of 1:16,383 (data acquisition system by G. W. Hannaway Assoc., Boulder, CO). Most commonly a Zeiss ×100, 1.4 numerical aperture objective was used in combination with a ×2.5 photo eye piece and an optivar setting of ×1.25 for a total magnification of ×312 at the camera (pixel size = 64 nm). We characterized the blurring introduced by the optics by measuring the point-spread function of the imaging system by acquiring a series of optical sections of a 0.2-μm-diameter fluorescent bead, using the same optical conditions as those used to obtain the cell image. By combining the optical sections of the cell with this quantitative calibration of the microscope blurring and the a priori information that the fluorescent dye density is nonnegative, we computationally reversed blurring in the cell image (*19*). We used L^2 regularization with nonnegativity constraint (*19*); this estimates the unknown dye density, f, as the nonnegative density that minimizes the expression

$$\Sigma|\text{image}(i,j,k) - \text{blur}(f)|^2 + \alpha\iiint|f(x,y,z)|^2\,dxdydz$$

where $\text{blur}(f)(i,j,k)$ is the value at voxel (i,j,k) of the function $f(x,y,z)$ computationally blurred by the point-spread function. The parameter, α, determines the smoothness setting of the restored image and is set at a level that avoids noisiness and graininess in the image.
21. D. L. Spector *et al.*, *EMBO J.* **10**, 3467 (1991).
22. D. L. Spector, *Proc. Natl. Acad. Sci. U.S.A.* **87**, 147 (1990).
23. Evidence that leads to the suggestion that there is a continuous 3-D nuclear reticulum of RNA splicing components is of two types: alkaline phosphatase detection with antibodies against snRNPs in serial electron microscopic sections (*22*) and immunofluorescence of SC-35 viewed by confocal microscopy (*21*). The precision of alkaline phosphatase detection is limited by the diffusion of the enzymatic reaction product [R. H. Singer *et al.*, *BioTechniques* **4**, 230 (1986)] and by the fact that the signals are amplified in an easily saturable manner, which can obscure differences in the relative quantities of molecules detected. Using high-resolution, high-magnification optics with confocal microscopy, we found regions of high-intensity poly(A) RNA or SC-35 signal to be discrete and generally not interconnected. However, as noted in Fig. 1, the limitations of confocal microscopy can make it more difficult, relative to the approach used here, to resolve closely spaced objects, and for any imaging system, the dynamic range and threshold chosen for display of information can substantially affect the definition of borders between regions of sharply different intensity.
24. In contrast to the transcript domains, single nucleoli occupied the upper and lower portions of the nucleus at equal frequency. A few cells (<5%) lacked such a ventral arrangement or had one or two domains clearly positioned in a plane above the others. The presence of these atypical cells indicates that there is some variation in the normal pattern and also shows, along with nucleolar localization, that the usual placement of these domains in the lower half of the nucleus is not because of bias introduced by the imaging techniques.
25. I. Petterson *et al.*, *J. Biol. Chem.* **259**, 5907 (1984).

26. J. Coleman and J. B. Lawrence, unpublished data.
27. L. E. Maquat, *Curr. Opin. Cell Biol.* **3**, 1004 (1991).
28. Y. Xing and J. B. Lawrence, *J. Cell Biol.* **112**, 1055 (1991).
29. W. G. Nelson *et al.*, *Annu. Rev. Biophys. Biophys. Chem.* **15**, 457 (1986); E. L. Fey *et al.*, *CRC Crit. Rev. Euk. Gene Express.* **1**, 127 (1991); D. A. Jackson, *BioEssays* **13**, 1 (1991).
30. Immunoelectron microscopy studies indicate that snRNPs and SC-35 localize to interchromatin granule clusters (*7, 21*). These clusters likely correlate with transcript domains, but their precise spatial relation remains unresolved, particularly with respect to their relative boundaries. Interestingly, the interchromatin granule clusters (which may be poly(A) RNA–rich) do not label as heavily as some other areas of the nucleoplasm when [^{3}H]uridine is incorporated into total nuclear RNA (*5*). Only a small fraction of nuclear RNA is heterogeneous nuclear RNA, and 80% of this fraction is not polyadenylated [B. Lewin, *Cell* **4**, 1 (1975)]. Much of this non-poly(A) RNA likely resides outside transcript domains as indicated by general RNA staining with fluorescent dyes (K. C. Carter and J. B. Lawrence, unpublished data).
31. Fixation, in situ hybridization, and fluorescence detection were done on the basis of our previously developed methods for the preservation and detection of cellular constituents including intact RNA [C. V. Johnson, R. H. Singer, J. B. Lawrence, *Methods Cell Biol.* **35**, 73 (1991)]. Cells were briefly treated with 0.5% Triton X-100 (<30 s), fixed in 2% or 4% paraformaldehyde (10 min), and stored in 70% ethanol. Poly(A) RNA detection with biotinylated deoxy(T)$_{55}$ and double-labeling of RNA and specific proteins were performed as described (*9*). Transcript domains were detectable in living cells and in cells fixed by a variety of methods (*9*), but it remains to be determined whether the finer details of the images shown here are dependent on the type of fixation.
32. G. J. Brakenhoff *et al.*, *J. Microsc.* (*Oxford*) **153**, 151 (1989).
33. We thank T. Maniatis for generous supplies of SC-35 and G. Blobel and T. Fey for generous supplies of nuclear pore antibodies; L. Lifshitz for useful discussion and development of software applications; C. Beaudry for help during manuscript preparation; M. Gerdes for technical assistance; and C. Dunshee for excellent photographic work and perseverance during figure compilation. Supported by NIH grant 2RO1HG00251, Research Career Development Award grant 5K04HG00002, and a Muscular Dystrophy Association grant (J.B.L.), NSF grant DIR8720188 (F.S.F.), and NIH fellowship 1F32HG00026 (K.C.C.).

14 July 1992; accepted 22 December 1992

TECHNICAL COMMENTS

The Role of Water in Hemoglobin Function and Stability

The report by M. F. Colombo *et al.* (*1*) and the Perspective by R. P. Rand (*2*) state that a large number of water molecules (about 60) take part in the allosteric regulation of human hemoglobin A (HbA). In our microscopic approach, published 1 year earlier (*3*), we derived not only the number of water molecules involved in the allosteric mechanism (about 75, the "correct" number being largely a matter of definition) but also their entropic contribution to the allosteric constant. To this purpose, we combined data about the viscosity and density of solutions of monohydric alcohols with earlier data from a study by L. Cordone *et al.* (*4*) concerning the effects of the same alcohols on the oxygen equilibrium of HbA. We used an extrapolation to zero alcohol concentration; Cordone *et al.* subtracted contributions resulting from changes in the dielectric constant in alcohol solutions. This procedure is at variance with Colombo *et al.*'s method of using considerable polysaccharide concentrations, which surely affect the dielectric constant. Also, we commented (*3*) on the significance of a (HbA + number of water molecules) unit. The latter (compared with the bare HbA) presents a greatly expanded set of microscopic states that concur in one and the same functional state (or set of functional states) (*3, 5*). This confers to the (protein + number of water molecules) unit the long-searched-for (*5*) thermodynamic stability of a semimacroscopic machine.

The enthalpic contribution of the approximately 75 water molecules to the allosteric mechanism has also been derived (*6*). In addition, recent simulations (*7*) and experiments on myoglobin (*8*) suggest that many more water molecules similarly contribute to forces responsible for the structure and dynamics of the whole protein. Such molecules would further extend the thermodynamic probability of the functional state of the (protein and water) system.

Solvent-induced forces (SIFs) are at least as important as other forces (for example, electrostatic) acting through the solvent (*9*). Perhaps, as a consequence of their subtle nature, SIFs are overlooked or related to some (ill-defined) "hydration water" that is erroneously supposed to have necessarily extra long residence or rotational times around solutes.

Average values of SIFs can be understood in terms of the solute-solvent potential energy, U_{SW}, and of its thermodynamic average, $\langle U_{SW} \rangle$, over all solvent configurations (*10*). In the averaging process the entropic contribution is brought in, so that $\langle U_{SW} \rangle$ measures the free energy of solute-solvent interactions. When the mutual presentation and distance (R) of two solutes is slowly varied from R_0 to R there is a change of free energy, $\Delta\langle U_{SW} \rangle$, resulting from work performed by SIFs in the change of mutual position. It follows that $\bar{F}_{q_i}$, the average SIF component acting between the given solutes along the q_i coordinate, is given by the derivative of $\langle U_{SW} \rangle$ along q_i. SIFs on a protein would change on the space scale of individual atoms or residues and on the time scale of the solvent rearrangement times among configurations available to the solvent. What counts in determining a given $\bar{F}_{q_i}$ are the structural and dynamic configurations available to the solvent (compatible with constraints imposed by the given and nearby solutes) and the *relative statistical weight* of these configurations, rather than the structural rearrangement time scale (*5, 11*). In itself, a change of the latter reflects changes of inherent structures (*12*) caused by the presence of solute or solutes (*11*).

SIFs also affect the overall thermodynamic stability of biomolecular solutions (*11, 13*). The instability regions (as encompassed by their respective spinodal lines) of solutions of HbA and hemoglobin S (HbS) in standard conditions, together with the similar region for HbA in high phosphate (*13*), are shown in Fig. 1. The location of these regions in the temperature–concentration plane indicates the tendency of solutions toward demixing, as distinct from gelation (*13, 14*). Instability regions are obtained by extrapolation from experiments in the accessible temperature interval (*13*). A mean-field approximation holds for the derivation of these spinodal lines (*13*), which allows quantitative values for Flory-Huggins enthalpies and entropies to be determined (*13*). Modulation of the solvent (by phosphate concentration) or the solute (by the Glu-Val substitution corresponding to the HbA-HbS mutation) affects both the instability region (a mean-field effect) and the molecular local recognitive interactions needed for the orderly self-assembly of the

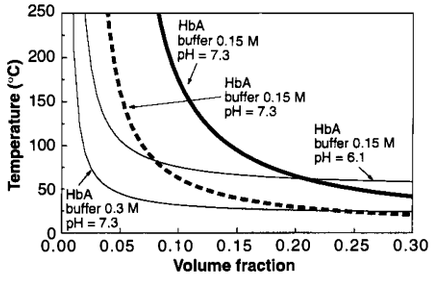

Fig. 1. Spinodal lines of solutions of human hemoglobins showing the lower temperature boundaries of the respective instability regions. Data from (*13, 16*). Gelation regions shown as gray and hatched areas, as given in (*15*).